RSC Advances

This article can be cited before page numbers have been issued, to do this please use: L. Kuang and W. Zhang, *RSC Adv.*, 2015, DOI: 10.1039/C5RA26096E.

ROYAL SOCIETY OF CHEMISTRY

www.rsc.org/advances

View Article Online
DOI: 10.1039/C5RA26096E

Enhanced Hydrogen Production by Carbon-doped TiO_2 Decorated with Reduced Graphene Oxide (rGO) under Visible Light Irradiation

Liyuan Kuang, Wen Zhang*

John A. Reif, Jr. Department of Civil and Environmental Engineering, New Jersey Institute of Technology, Newark, NJ 07102

*Corresponding author: e-mail: wzhang81@njit.edu; Phone: 1-973-596-5520; Fax: 1-973-596-5790.

Abstract. Enhancing visible light utilization by photocatalysts, avoiding electron-hole recombination, and facilitating charge transfer are three major challenges to the success of sustainable photocatalytic systems. In our study, carbon-doped TiO_2 was synthesized with decoration of reduced graphene oxide (C-TiO_2/rGO) to form a hybrid nanocomposite that exhibits excellent photocatalytic activity and longevity. Morphology, chemical and colloidal stability, crystallinity, surface compositions and band structures were systematically assessed. The results revealed that the hybrid C-TiO_2/rGO had a band gap of 2.2 ± 0.2 eV and crystallite sizes of 0.9–2 nm in diameter. Transmission electron microcopy (TEM) images showed that C-TiO_2 particles attached to the carbon sheet of rGO. Under irradiation of 135 $mW \cdot cm^{-2}$ at 400–690 nm with methanol as electron donor, C-TiO_2 and C-TiO_2/rGO yielded incredibly high H_2 production rates of 0.67 ± 0.12 to 1.50 ± 0.2 $mmol \cdot g^{-1} \cdot h^{-1}$, respectively, which were greater than those of other titanium hybrid catalysts such as C-TiO_2 and C-TiO_2/Pt. rGO not only greatly improved the photocatalytic activity but also led to greater stability of H_2 production compared to C-TiO_2. This work lays groundwork toward the design of novel visible light-driven photocatalytic systems for harnessing solar energy and environmental applications.

Keywords: TiO_2, carbon doped TiO_2, graphene oxide, reduced graphene oxide, visible light photocatalysis, H_2 production.

View Article Online
DOI: 10.1039/C5RA26096E

1. Introduction

Visible light-driven photocatalytic hydrogen (H_2) production presents an appealing approach to harness solar energy and potentially tackles many environmental issues such as wastewater treatment.[1-3] Efficient photocatalytic H_2 production require efficient and stable photocatalysts that could maintain excellent photocatalytic activity and longevity. Most traditional photocatalysts (e.g., TiO_2) have relatively large band gaps (>3 eV) and thus can only capture ultraviolet (UV) irradiation[4], which accounts for about 5% of solar irradiation. To effectively capture visible light from solar spectrum, photocatalytic materials should have band gaps in the 1.6–1.9 eV range.[5] Thus, band engineering is the typical strategy to broaden visible light utilization, while retaining excellent electron-hole separation and stability of photocatalytic reactions.[6]

Elemental doping is one of the band engineering methods that incorporate metal ions, nonmetal ions, and metal/nonmetal ions into catalyst synthesis.[7-9] Metal ions such V, Ni, Cr, Au, Ag, Mo, Fe, Sn, and Mn were previously used.[10-13] Non-metals such as C, N, and S have been widely used to shift the valence band edge upward and thus narrow band gaps.[14-16] For instance, Asahi et al. studied the substitutional doping of C, N, F, P, and S for O in anatase TiO_2.[17] Chen and co-workers used X-ray photoelectron spectroscopy (XPS) to demonstrate the presence of additional electronic states above the valence band edge of C-, N-, and S-doped TiO_2.[8, 18] The additional electron density of states explained the red shifted absorption as observed in the "shoulder" and "tail-like" features in the UV-vis spectra of these modified photocatalysts. Particularly, carbon doping has proved to be effective in narrowing band gap of TiO_2.[8, 14, 17, 19, 20] Particularly, carbon-doped TiO_2 (C-TiO_2) was shown to be the best in narrowing energy bandgap.[21] C-TiO_2nanotubes also displayed a high photoactivity for water splitting and

View Article Online
DOI: 10.1039/C5RA26096E

utilization of solar energy up to the visible to infrared region, due to band gap reduction and the new intragap band formation. However, the current challenges for these doped Ti-based photocatalysts are the rapid electron−hole recombination,[22] followed by quantum yield,[23] stability,[23, 24] and synthesis cost. One of the strategies for preventing the recombination is to build heterojunctions containing anion-doped titania and to coat or decorate metal or semiconductor nanomaterials or organic dye photosensitizers to facilitate electron–hole separation.[25, 26]

Carbonaceous nanomaterials such as carbon nanotubes,[27] graphene or graphene oxide (GO)[28, 29] have been integrated in the synthesis of novel nanocomposites with improved performance of photocatalysts,[30, 31] fuel cells,[32] and batteries,[33] where charge separation and electron transport are dominant operating principles. Graphene, for instance, provides a unique two-dimensional (2-D) platform for electron transport with a high specific surface area (up to 2630 $m^2 \cdot g^{-1}$) with exceptional chemical and mechanical stability, electrical conductivity and electron mobility (~200,000 $cm^2 \cdot V^{-1} \cdot s^{-1}$).[34] Anchoring photocatalysts onto graphitic nanostructures could also cause a red-shift in the absorption spectrum,[35, 36] as well as prevention of catalyst aggregation.[37] Reduced graphene oxide (rGO) greatly restores a high degree of the sp2 bonding structure inherent to pristine graphene and yields a conductive 2-D carbon mat that can shuttle charges between the active nanostructured materials.[38] Previous work employed rGO as a supporting matrix for TiO_2 and achieved good photocatalytic performance under UV-vis irradiation.[39] However, the roles of rGO in visible-light-driven photocatalytic H_2 evolution as well as in photochemical or colloidal stability of hybrid nanostructures of doped titania have not been well elucidated (See the summary of recent studies in **Table 1**). As opposed to doping rare earth elements, noble or transition metals such as Pt, Pd, Ru and Rh, non-metal co-catalysts (e.g.,

View Article Online
DOI: 10.1039/C5RA26096E

nitrogen-doped GO[40]) are shown to be more sustainable because carbon or nitrogen elements are earth abundant,[41] and some heavy metal dopants such as Cr and Cd are toxic and harmful to ecosystems and the environment, which limits their wide application.[42]

In this study, C-TiO_2 was synthesized and further anchored to rGO to create hybrid nanocomposites (C-TiO_2/rGO) for H_2 production under visible light irradiation. TiO_2 was used as a base photocatalytic material mainly because of its excellent photoreactivity, chemical stability (no dissolution or ion release), facile synthesis, low cost, and relative nontoxicity. Material properties such as morphology, chemical and colloidal stability, crystallinity, surface compositions and band structure were systematically assessed. We compared the photocatalytic H_2 production rates for C-TiO_2 and C-TiO_2/rGO and further evaluated the longevity of C-TiO_2/rGO. The role of rGO in improving photocatalytic activity and mechanisms of photocatalytic reactions were analyzed to provide insight into the design of novel visible light-responsive photocatalysts.

Table 1. Comparison of literature on visible light-driven H_2 production by titania based catalysts with or without graphene.

Catalyst	Light source (nm)	Electron donor	Light intensity ($mW \cdot cm^{-2}$)	Average H_2 Productivity			Longevity of each reaction cycle (h)	Ref.
				$\mu mol \cdot L^{-1} \cdot h^{-1}$	$mmol \cdot g^{-1} \cdot h^{-1}$	$\mu mol \cdot m^{-2} \cdot h^{-1}$		
GSs/TiO_2	Xe lamp	Na_2S/Na_2SO_3	150	43	0.086	NA	NA	39
TiO_2/G	UV-Vis	Na_2S/Na_2SO_3	80	27	0.108	NA	5	25
TiO_2/G	Xe lamp	Methanol	NA	11133	6.68	119.07	9	43
TiO_2/rGO	UV-Vis	Methanol	NA	740	0.74	NA	3 (4 runs)	44
TiO_2/rGO	> 320	Methanol	205	NA	NA	NA	NA	45
Cu_2O-TiO_2/rGO	Xe lamp	Glycerol	NA	NA	110.968	NA	8 h	46
Eosin Y-Pt-N-TiO_2	> 420	TEOA	NA	1000	0.8	8.7	NA	47
g-C_3N_4/N-TiO_2 nanofibers	Xe lamp	Methanol	NA	3572.52	8.93	NA	NA	48
Ce-N-TiO_2	Tungsten halogen lamp	Methanol	NA	8240	1.03	NA	NA	49
Ce-B-TiO_2	Tungsten halogen lamp	Methanol	NA	6334.5	0.79	NA	NA	49
Ce-C-TiO_2	Tungsten halogen lamp	Methanol	NA	5407.5	0.68	NA	NA	49
Ce-S-TiO_2	Tungsten halogen lamp	Methanol	NA	1287.5	0.16	NA	NA	49
N-TiO_2/N-GO	Hg lamp	Methanol	NA	906.18	0.996	NA	NA	50
Au/N-TiO_2	Xe lamp	Methanol	NA	8252	8.252	NA	NA	51
N-TiO_2	Xe lamp	Methanol	NA	2980	2.98	NA	NA	52
Pt/N-TiO_2	Solar simulator	Methanol	50	205.8	0.2	NA	NA	53
N-TiO_2	Xe lamp	NA	NA	NA	0.00003	NA	NA	54
Pt/N-TiO_2	Xe-arc lamp	Methanol	NA	1036.36	0.57	NA	NA	55
C,N-TiO_2	Xe lamp	Methanol	NA	105.55	0.081	0.89	NA	56
W/N-TiO_2	Vis	Ethanol	NA	43.88	0.0176	NA	NA	57
C-TiO_2/rGO	Xe lamp	Methanol	135	495	1.5	NA	20	This study
C-TiO_2	Xe lamp	TEOA	135	16.25	0.049	NA	NA	This study
C-TiO_2/rGO	Xe lamp	TEOA	135	21.67	0.066	NA	NA	This study

*G denotes graphene. rGO denotes reduced graphene oxide. GSs denotes graphene sheets.

View Article Online
DOI: 10.1039/C5RA26096E

2. Experimental

2.1. Synthesis of C-TiO_2/rGO

C-TiO_2 was synthesized via a reported one-pot solvothermal process with minor modifications to create nano-sized C-TiO_2.[20] Briefly, 2 ml of titanium isopropoxide was mixed with 60 ml of anhydrous acetone. The mixture was stirred at ambient conditions for 30 min and then transferred to a 125-ml Teflon-lined stainless-steel autoclave (Parr Instrument Co.) for heating at 200^{o}C for 12 h. After synthesis, the white precipitate was separated by centrifugation (2000×*g* for 10 min) and washed several times with deionized (DI) water. The precipitate then went through 2-h calcination in a furnace at 200 ^{o}C subsequently. Compared to other carbon doping methods, such as exposing TiO_2 to CO_2 or air at high temperatures,[58-63] the one-pot hydrothermal method we employed relied on relies on the aldol condensation reaction between titanium alkoxide and acetone,[20] which was reported to lead to high surface area, tunable pore and grain sizes, and high crystallinity elsewhere.[64]

GO was synthesized by the simplified Hummer's method,[65] which is described in details in supporting information (SI). C-TiO_2/rGO was obtained also via hydrothermal synthesis with a rGO loading ratio of 2%, which was optimized in previous studies.[25, 41] Briefly, 10 mg GO was dispersed in a solution of DI water (20 mL) and ethanol (30 mL) by 100-W ultrasonic treatment for 1 h. Then, 0.5 g C-TiO_2 was added to the obtained GO suspension and stirred for another 2 h to get a homogeneous suspension. The suspension was then placed in a 150-mL Teflon sealed autoclave and heated at 120 ^{o}C for 3 h to simultaneously achieve the reduction of GO and the deposition of C-TiO_2 on the rGO sheet. Finally, the resulting nanocomposite was purified and separated by filtration (0.2-micron Nylon Millipore filter), followed by rigorous DI water rinsing

View Article Online
DOI: 10.1039/C5RA26096E

and air drying at room temperature. rGO was obtained by the same procedure without adding C-TiO_2.

2.2. Characterization

Morphology and size distribution were determined by a Hitachi H-7500 transmission electron microscope (TEM). Hydrodynamic particle size distribution (PSD) and zeta potential were measured by dynamic light scattering (DLS) on a Zetasizer nano ZS instrument (Malvern Instruments, UK). X-ray Diffraction (XRD) was recorded for the crystallography using a Philips PW3040 X-Ray Diffractometer. Surface compositions and crystalline phases were assessed by Fourier Transform Infrared (FTIR) and Raman Spectrometers. FTIR was performed on a Nicolet Thermo Electron FTIR spectrometer combined with a MIRacle attenuated total reflectance (ATR) platform assembly and a Ge plate, while Raman was carried out with a Thermo Scientific DXR Raman microscope using an argon ion laser excitation (λ=514.5 nm) at powers of 2-10 mW. The thermal behavior of our composite catalysts with rGO was analyzed by a temperature programmed desorption (TPD) technique on a Micromeritics® AutoChem II 2920 system with a mass spectrometer (SRS QMS200). The UV-Vis absorption spectra were obtained using a Thermo scientific Evolution 201PC spectrophotometer.

2.3. Photocatalytic H_2 production

Photocatalytic reactions were carried out in a 250-mL Pyrex flask reactor, which was sealed with a silicone rubber septum. The visible light irradiation between 400 nm and 690 nm was provided by a 300-W Xe lamp (PerkinElmer, PE300BF). The light intensity at the reaction suspension was maintained at approximately 135 $mW \cdot cm^{-2}$ (the exposure area was about 7 cm^2), measured by a spectroradiometer with a waterproof probe (Spectral Evolution, SR-1100). In the photocatalytic H_2 reactions, the catalyst suspension was made by dispersing 0.066 g of the

View Article Online
DOI: 10.1039/C5RA26096E

catalyst (C-TiO_2 or C-TiO_2/rGO) in 200 mL of DI water with methanol as electron donor at an initial concentration of 25% v/v or 197.95 $g \cdot L^{-1}$ (pH = 5.2). The suspension was mixed continuously using a magnetic stirrer. Before exposure to irradiation, the system was purged with N_2 gas for at least 30 min to remove dissolved oxygen. All measurements of produced H_2 concentrations at different irradiation times were performed three times to confirm the significance of the presented data and report the mean values with standard deviation as error bars. The H_2 concentration in gas phase of the overhead space was determined with gas chromatography (Agilent GC-5890) using HP-MS5 column, TCD, and N_2 as the carrier phase. Quantum yield was calculated following the method reported elsewhere.[66-68]

In the assessment of longevity, the same photocatalytic reactions were conducted for multiple cycles (a cycle is defined as the period, in which photocatalytic H_2 production started and terminated due to pseudo equilibrium). After each cycle, we used N_2 to purge the suspension at least 30 min to remove the aqueous- and air-phase H_2. Then, the illumination was turned on to resume photocatalytic H_2 production.

3. Results and Discussion

3.1. Morphology and particle size distribution.

Figure 1a-1c shows the TEM images of rGO, C-TiO_2, and C-TiO_2/rGO. GO and rGO have crumpled layered structures with irregular shapes or sizes (also see **Figure S1** for more pictures of these materials). The Energy-dispersive X-ray spectroscopy (EDS) result in **Figure S2** indicated that the mass percentage of carbon dopant in C-TiO_2 was approximately 2.32 %. **Figure 1b** shows C-TiO_2 nanocrystals aggregated into big clusters. **Figure 1c** shows C-TiO_2 nanocrystals were anchored onto the carbon sheet of rGO. Individual particles of C-TiO_2 had 9.1± 3.3 nm in diameter determined from TEM images with the size distribution shown in

View Article Online
DOI: 10.1039/C5RA26096E

Figure 1d, which is consistent with the literature.[20] Furthermore, the Scherer's equation was used to compute the crystallite size of C-TiO_2 based on the XRD pattern indexed at (101), (004), (200), and (105). The calculated crystallite sizes ranged from 0.9 nm to 2 nm, indicating C-TiO_2 was likely polycrystalline.

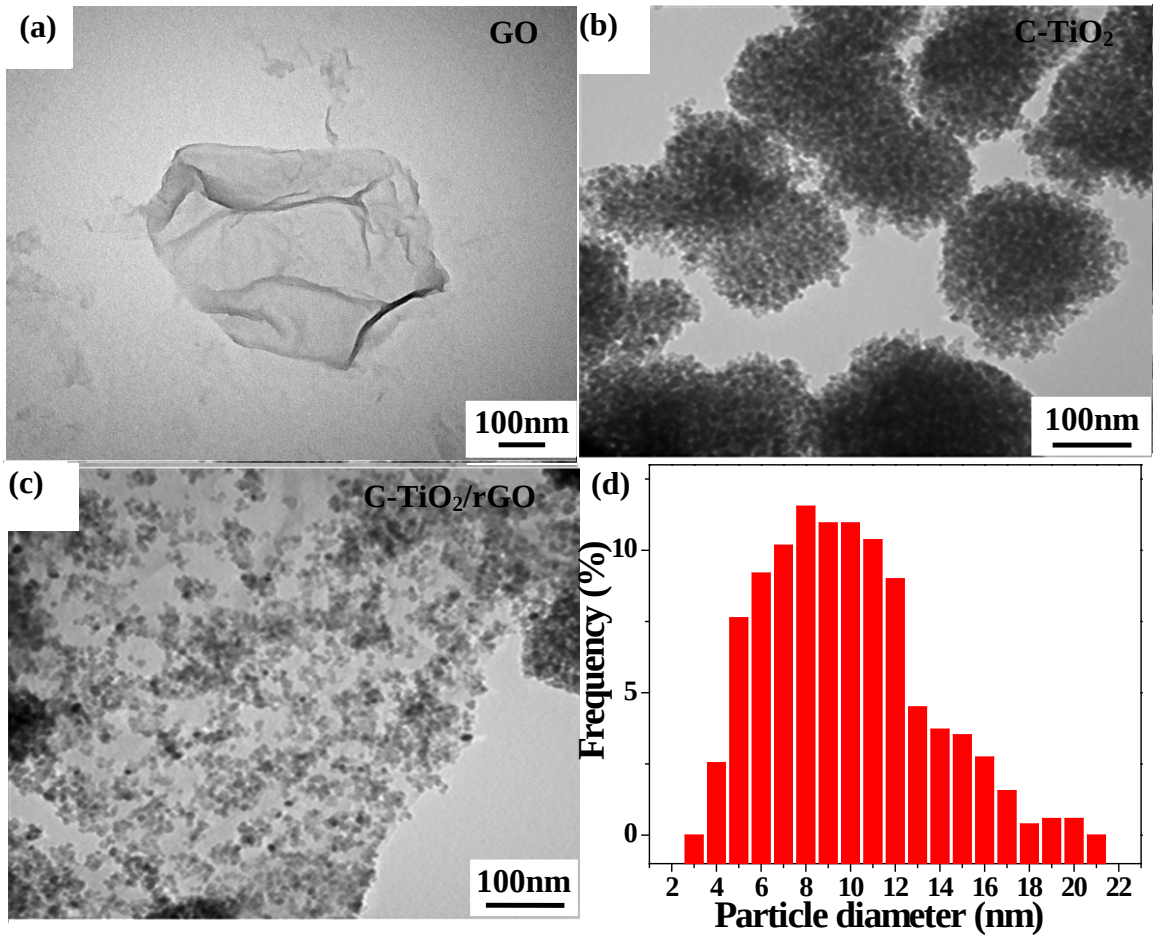

Figure 1. (a-c) TEM images of GO, C-TiO_2 and C-TiO_2/rGO. (d) PSD of C-TiO_2 determined by ImageJ on TEM images (n=511).

3.2. Hydrodynamic diameters and zeta potentials.

The hydrodynamic size distributions and zeta potentials influence colloidal interactions and stability of dispersed photocatalysts. **Figure 2a** shows the PSD of the as-synthesized C-TiO_2, C-TiO_2/rGO, and rGO in DI water dispersion, which all exhibited bimodal size distribution. Hydrodynamic sizes of C-TiO_2 or C-TiO_2/rGO appear to be greater than those determined by

View Article Online
DOI: 10.1039/C5RA26096E

TEM probably because of aggregation and tendency of DLS to measure large colloids.[69] GO had a mean hydrodynamic diameter of about 44 nm, whereas rGO had two peaks at 1480 nm and 4800 nm, which was also reported else.[70]

Figure 2b shows zeta potentials of GO/rGO, C-TiO_2 and C-TiO_2/rGO measured in solutions of different pH (1.5–11.06). Due to the ionization of the multiple surface oxygenated functional groups, GO and rGO exhibited negative charges (e.g., -40 to -50 mV at neutral pH), which is consistent with other studies.[71] C-TiO_2 and C-TiO_2/rGO were positively charged at pH lower than 4 and 5 respectively. As discussed later, carbon dopants likely substituted oxygen atoms in TiO_2 (**Figure 3a**) and trap excessive electrons,[72] which led to a more negative charged surface for C-TiO_2. By contrast, P25 TiO_2 is usually more positively charged at pH 4-5.[73] At higher pHs, they both shifted to negative charges, which is in agreement with other reports.[74] The isoelectric point of C-TiO_2 and C-TiO_2/rGO was 4.3 and 5.2, respectively. The difference was clearly caused by rGO decoration. Moreover, zeta potential of C-TiO_2 and C-TiO_2/rGO in 25% methanol solution (pH= 5.3) used in our photocatalytic experiments was -0.5 ± 0.6 mV and 14.0 ± 0.6 mV, respectively. A greater positive charge for C-TiO_2/rGO was observed although C-TiO_2 or rGO both had less positive or even negative charges at the pH range of 4-5. The possible reason for this unexpected positive charge is that after conjugation with C-TiO_2, rGO sheets were probably functionalized by some Ti cations as illustrated in **Figure 3b**.[75]

View Article Online
DOI: 10.1039/C5RA26096E

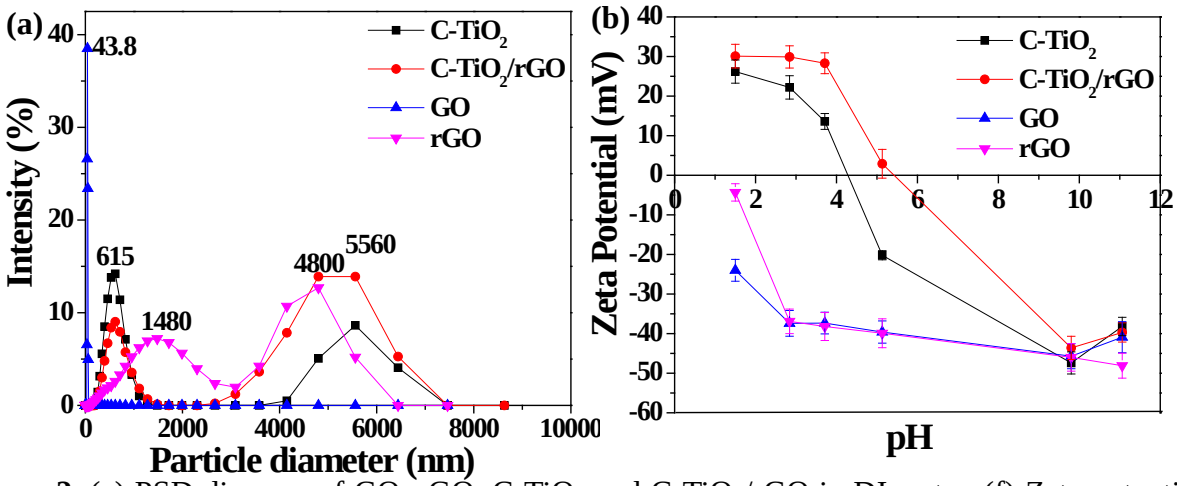

Figure 2. (a) PSD diagram of GO, rGO, C-TiO_2 and C-TiO_2/rGO in DI water. (f) Zeta potential of C-TiO_2, C-TiO_2/rGO, GO and rGO as a function of pH in DI water.

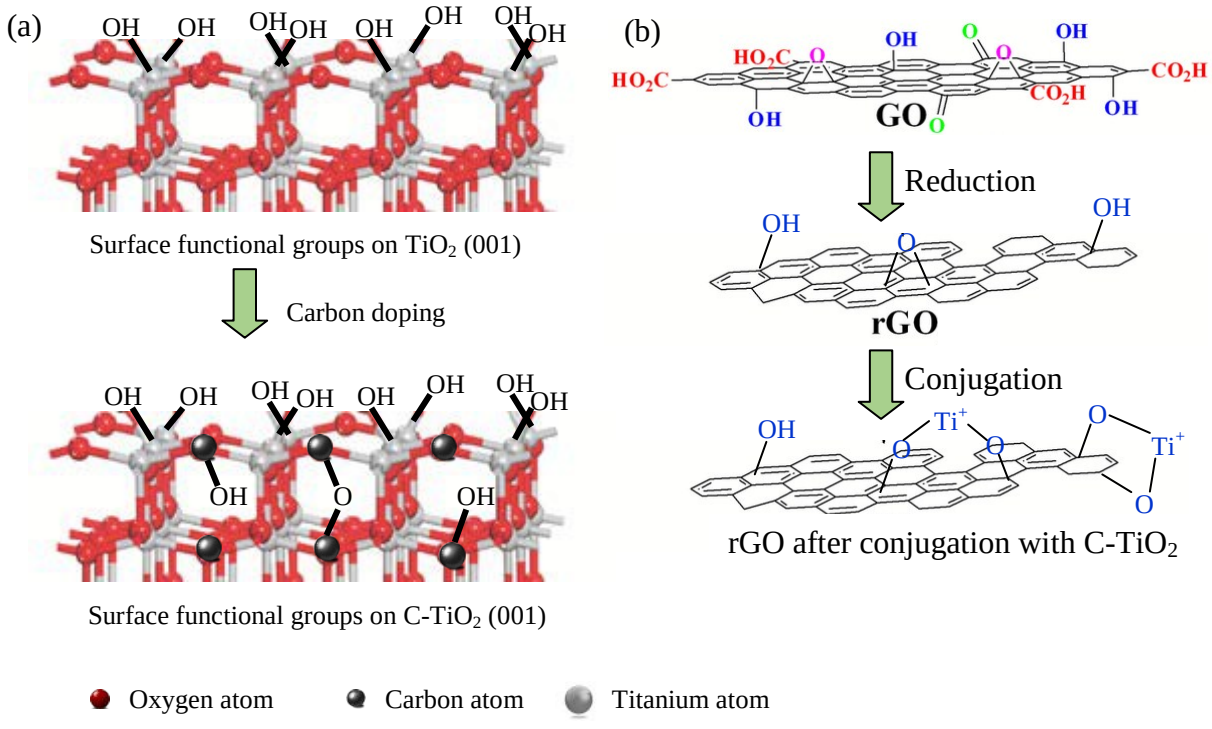

Figure 3. Surface functional group variations on (a) TiO_2 and C-TiO_2 and (b) GO, rGO, and rGO conjugated with C-TiO_2.

View Article Online
DOI: 10.1039/C5RA26096E

3.3. Crystallinity.

XRD patterns in **Figure 4** show that anatase TiO_2 was the main polymorph present in the samples of C-TiO_2 and C-TiO_2/rGO with indexed peaks at (101), (004), (200), (105), (211), (116), (220) and (215) with increasing diffraction angles. These diffraction angles also indicate a body centered tetragonal crystalline structure of TiO_2.[76] The spectral shift of C-TiO_2 compared to commercial P25 TiO_2 (Product #: 637254, Aldrich, USA) implies that oxygen atoms in the TiO_2 could be substituted by carbon atoms.[20, 76] No apparent rGO peak in the C-TiO_2/rGO sample suggested that C-TiO_2 particles may have largely deposited on the surface of rGO and suppressed the XRD signal from the stacking of rGO layers.[77]

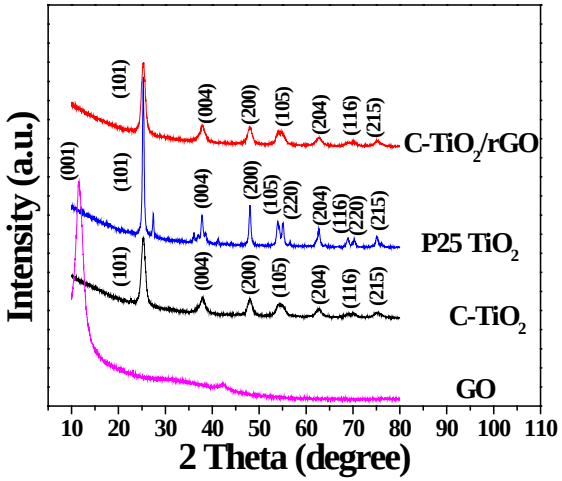

Figure 4. XRD pattern for GO, TiO_2, C-TiO_2 and C-TiO_2/rGO.

3.4. Surface compositions.

Figure 5 shows the FTIR spectra of GO, rGO, C-TiO_2 and C-TiO_2/rGO. The unique absorption peaks of GO included 1027 cm^{-1} for C-O stretching,[78] 1217 cm^{-1} for phenolic C-OH stretching,[79] 1609 cm^{-1} for the hydroxyl groups of molecular water,[80] and 1711 cm^{-1} for C = O stretching.[81] The intensities of absorption bands of oxygen-containing functional groups such as C-O (1052 cm^{-1}) on rGO were dramatically reduced compared with GO. The C-OH at 1217

View Article Online
DOI: 10.1039/C5RA26096E

cm^{-1} and 1609 cm^{-1} for the hydroxyl groups of molecular water were still found on C-TiO_2/rGO, implying that GO was only partially reduced to rGO by the solvothermal treatment. The strong adsorption at 600 cm^{-1} found on C-TiO_2 and C-TiO_2/rGO was due to the Ti-O-Ti bond.[80]

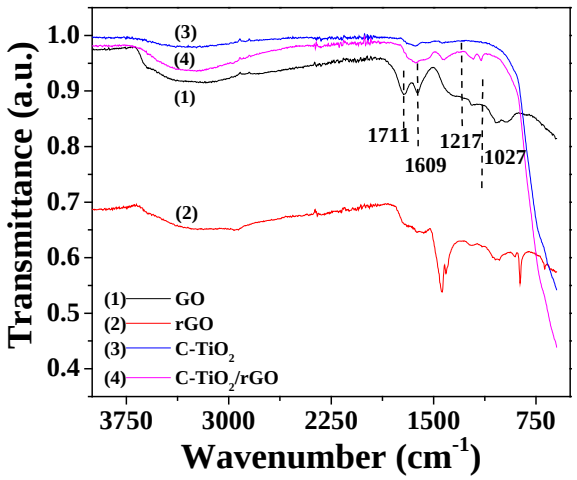

Figure 5. FTIR spectra for C-TiO_2, C-TiO_2/rGO, GO and rGO.

3.5. Raman spectra.

Figure 6 shows the Raman spectra for C-TiO_2 and C-TiO_2/rGO both displayed active modes at Eg (143 cm^{-1}), Eg (196 cm^{-1}), B1g (398 cm^{-1}), A1g (518 cm^{-1}) and Eg (637 cm^{-1}),[82, 83] which are related to the tetragonal structure of anatase TiO_2 with a D4h space group.[84] Thus, Raman spectra also confirmed our synthesized C-TiO_2 catalysts were crystallized in anatase phase of TiO_2.[85] Two characteristic peaks of GO or rGO located at about 1361 and 1590 cm^{-1} correspond to disorder carbon (D-band) and graphite carbon (G-band) were observed, respectively. C-TiO_2/rGO yielded the same two bands, proving the existence of rGO in the composite. These bands correspond to the E_{2g} phonon of sp^2-bonded carbon atoms in a two-dimensional hexagonal lattice, as well as the defects and disordered carbon in the graphite layers, respectively. The D/G intensity ratio (0.98) of C-TiO_2/rGO was slightly larger than that (0.91) of rGO itself, suggesting a decrease in the average size of the sp2 domains upon reduction of the exfoliated GO. Generally,

View Article Online
DOI: 10.1039/C5RA26096E

a Lorentzian peak for the 2D band of the monolayer graphene sheets is observed at 2679 cm^{-1}, whereas this peak may be broaden and shifted to higher wavenumber in case of multi-layer graphene.[86] In this study, the 2D band was not observed for GO or rGO, or C-TiO_2/rGO, which indicates that the tested GO and rGO may have a monolayer structure and C-TiO_2/rGO had no stacking structures.[87]

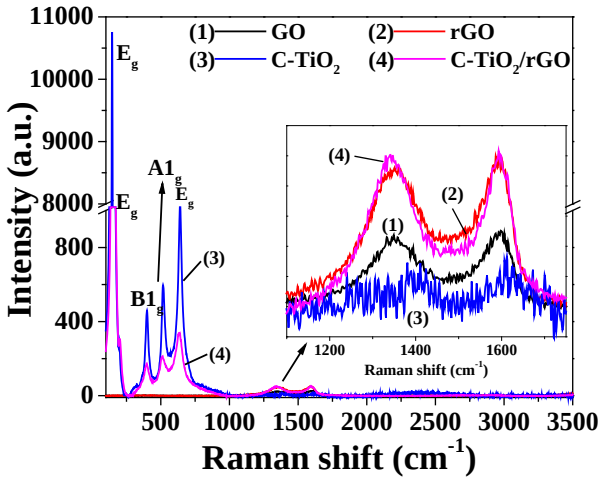

Figure 6. Raman spectra of GO, rGO, C-TiO_2, and C-TiO_2/rGO.

3.6. Thermal behavior.

The TPD system heated up P25 TiO_2, C-TiO_2, C-TiO_2/rGO, GO and rGO from room temperature to 800 ^oC at a heating rate of 10 $^oC \cdot min^{-1}$ under the flowing of helium. **Figure 7** shows that only GO and rGO released CO_2 at around 215 °C owing to decomposition of carboxyl functional groups,[88] while all other except P25 TiO_2 released significant amounts of H_2O at 130 ^oC and 250 ^oC due to the loss of surface moisture and chemically bounded waters. Particularly, GO released a greater amount (mM-CO_2·mg-GO or rGO) of CO_2 than rGO (**Figure 7a**), indicating that rGO had a considerably reduced content of oxygen after hydrothermal treatment.

View Article Online
DOI: 10.1039/C5RA26096E

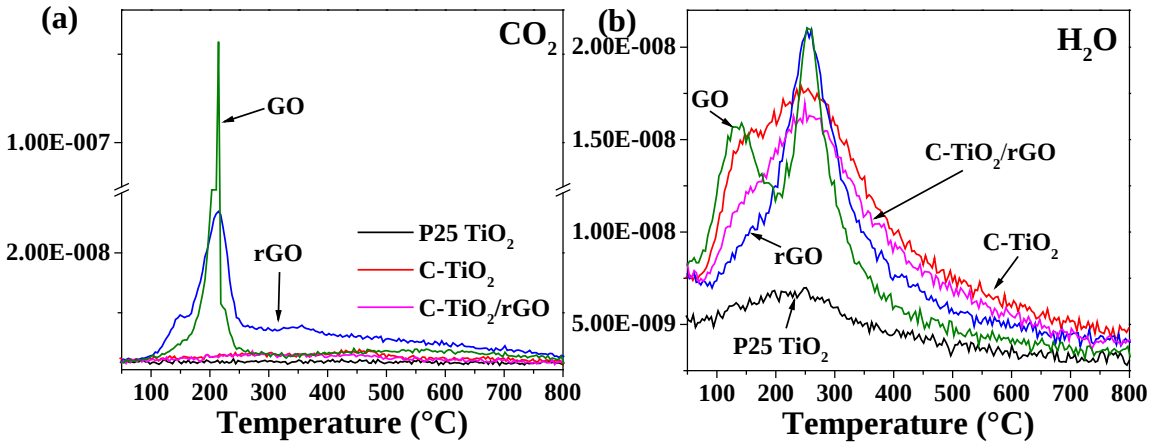

Figure 7. Mass loss of the relevant molecular fragments in TPD analysis.

3.7. Band structures.

To compare the band gaps of P25 TiO_2, C-TiO_2, and C-TiO_2/rGO, UV-Vis diffuse reflectance absorption spectra were obtained for their water dispersion as shown in **Figure 8a**. GO and P25 TiO_2 exhibited stronger absorption in UV region than in visible light region. Conversely, the absorption bands for C-TiO_2 or C-TiO_2/rGO shifted to the visible light region. According to the Kubelkae-Munk function, the band gap can be determined from the plot $(\alpha h\nu)^2$ versus the energy of exciting light ($h\nu$).[66-68, 89] Here, α is the absorption coefficient and $h\nu$ is the photon energy. Based on linear extrapolation (dotted lines) in **Figure 8b**, the band gaps of P25 TiO_2, C-TiO_2 and C-TiO_2/rGO was determined to be approximately 3.0 eV, 2.5 eV, 2.2 eV, respectively, which correspond to the wavelengths of 443 nm, 539 nm, and 620 nm. Clearly, carbon doping narrowed the band gap of TiO_2, which effectively enables the absorption of visible light. Computational chemistry modeling suggested carbon doping may result in the formation of oxygen vacancies, which could trap excess electrons at the empty p state of the embedded C atoms of $TiO_{2-x}C_x$. C-TiO_2 had a slightly narrower band gap than C-TiO_2/rGO due to the presence of rGO.[90] The presence of rGO clearly interfered the light absorbance of C-

View Article Online
DOI: 10.1039/C5RA26096E

TiO_2/rGO and therefore changed the apparent band gap of the hybrid structure. The bandgap of GO or rGO can vary from 0 to 4 eV depending on oxygen content or coverage.[91] That is why there are no sharp adsorption edges for a precise gap energy, because GO could have different oxidation levels.[92] From the approximate linear extrapolation, the synthesized GO had 2.7 eV-3.9 eV for direct transition as indicated by the dotted line on the red curve in **Figure 8b**, which are consistent with other studies.[91, 92]

For pure anatase TiO_2, the conduction band minimum (E_C) and the conduction band maximum (E_V) is about –0.37 V (vs. NHE) and +2.83 V (vs. NHE), respectively.[93] The doping of non-metals in TiO_2 lattice results in an upward shift of E_V, due to the contribution of 2p or 3p orbital of doped atoms.[94] The shift for C-doping originates from mixing the C2p states with the valence band of TiO_2. The intimate contact between rGO and C-TiO_2 should form a heterojunction or a Schottky junction due to their different work functions (E_f).[95, 96] As shown in **Figure 8c,** C-TiO_2 had upward band bending at the interface so that excited electrons flew from the conduction band of C-TiO_2 to rGO and from there they spread out and react with water or H^+ to form H_2.[97] In addition, rGO in the nanocomposites was reported to act as an organic dye-like macromolecular 'photosensitizer'.[98] Upon visible light irradiation, rGO may also produce photogenerated electrons that could be transferred to the conduction band of C-TiO_2 and thus improve the photocatalytic activity.

View Article Online
DOI: 10.1039/C5RA26096E

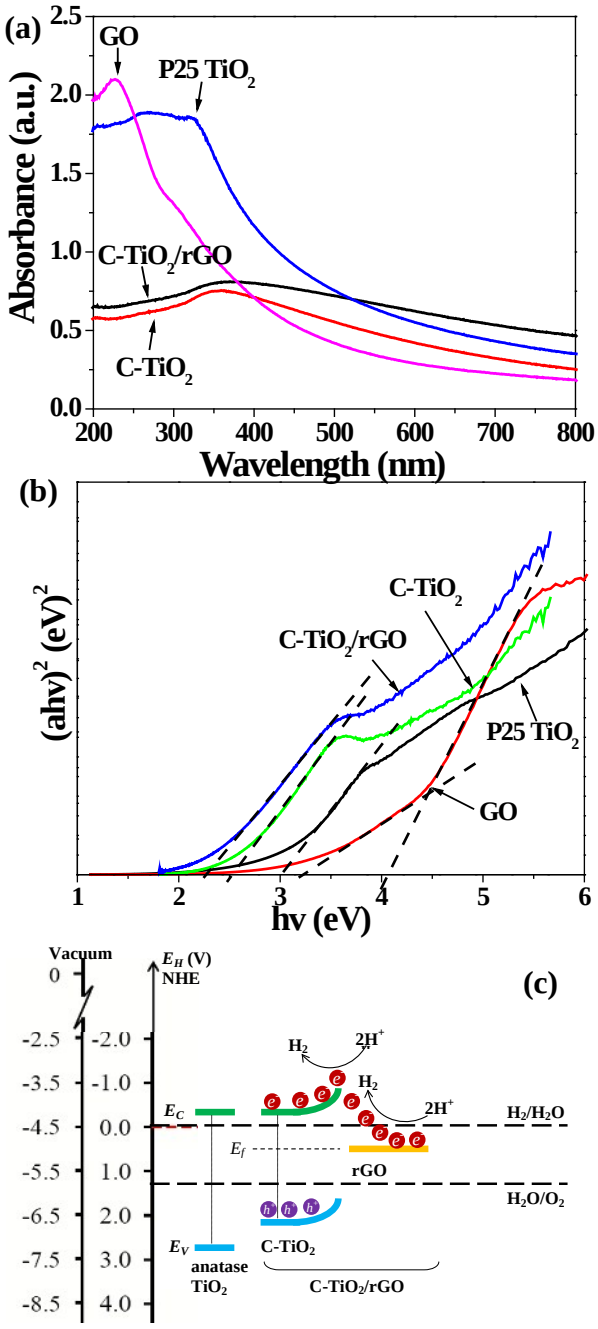

Figure 8. (a) UV-Vis absorbance spectrums for GO, TiO_2, C-TiO_2, and C-TiO_2/rGO. (b)The band gap values from the plots of $(\alpha h\nu)^2$ versus hν TiO_2 and C-TiO_2-rGO (2% loading). (c) The energy level diagram of a Schottky junction with respect to the normal hydrogen electrode (NHE) and the absolute vacuum scale (AVS) as references (pH=0). The upward band bending in an n-type semiconductor (C-TiO_2) at a heterojunction with rGO.

View Article Online
DOI: 10.1039/C5RA26096E

3.8. Photocatalytic H_2 production and stability.

The photocatalytic H_2 production was performed only with C-TiO_2 and C-TiO_2/rGO, whereas P25 TiO_2 or P25 TiO_2/rGO were not tested because they were unable to produce H_2 under visible light irradiation. **Figure 9** shows the photocatalytic H_2 production by C-TiO_2 and C-TiO_2/rGO as a function of irradiation time. The generated H_2 were accumulating at stable rates during the initial 6 h. The H_2 production rates significantly increased from 0.67 ± 0.12 to 1.50 ± 0.2 mmol·g-catalyst^{-1}·h^{-1} for C-TiO_2 and C-TiO_2/rGO respectively, the quantum yield improved from 4% to 10%, indicating that rGO greatly improved the photocatalytic activity. rGO was reported to form Ti-O-C bonds and facilitate both electron migration and efficiency of charge separation.[99] The photoexcited electrons in C-TiO_2/rGO could readily transfer from the conduction band of C-TiO_2 to a graphene acceptor via percolation mechanism,[100] therefore promoting the H_2 production. This production rate is even higher than other titanium hybrid catalysts with noble metals as co-catalyst such as TiO_2/Pt or C-TiO_2/Pt (0.02−7 mmol-H_2 ·g^{-1}·h^{-1}).[101-103] Moreover, in addition to methanol, another common organic electron donor, triethanolamine (TEOA) was also used and shown to produce H_2 at a rate of approximately 0.05−0.07 mmol-H_2 ·g^{-1}·h^{-1} with our C-TiO_2 and C-TiO_2/rGO catalysts (**Figure S3**).

The stability of photocatalytic H_2 production over multiple reaction cycles was examined on C-TiO_2 and C-TiO_2/rGO to provide new insight into the reaction design. **Figure 9b** and **9c** shows the H_2 production scenarios for multiple reaction cycles. The reaction cycle ended when a pseudo equilibrium reached. More than 90% of spiked methanol (~188.5 g·L^{-1}) still remained in the suspension. Therefore, the catalyst suspension was purged by N_2 gas for 30 min to expel aqueous phase H_2 or CO_2, which was shown effective for rebooting the photocatalytic reaction. The photocatalytic H_2 rate for C-TiO_2 dramatically declined after one cycle (**Figure 9b**). By

View Article Online
DOI: 10.1039/C5RA26096E

contrast, C-TiO_2/rGO maintained fairly stable rates of H_2 production for several cycles (**Figure 9c**). For instance, the H_2 production rate decreased from 0.058 ± 0.02 , to 0.038 ± 0.03 mmol·h^{-1} after seven reaction cycles, highlighting the robust stability of C-TiO_2/rGO hybrid composite over C-TiO_2. To confirm the changes to colloidal stability after several consecutive reaction cycles, we also measured the zeta potentials and PSD in the reaction suspension, which remained almost the same as **Figure 2**. This observation highlights the unparalleled stability and resistance to photocorrosion of C-TiO_2 as compared to other sulfide catalysts such as CdS or ZnS.

The decline of photocatalytic H_2 production rates could be explained from the reaction mechanisms or stoichiometry as listed in ESI.[23] Methanol as electron donor or sacrificial species are oxidized by the photogenerated holes or radicals such as •OH into formaldehyde (HCHO), formic acid (HCOOH) and CO_2 ultimately. Photoexcited electrons in the conduction band reduce water or H^+ in the solution to form H_2. The product accumulation may slow down or even inhibit the photocatalytic reaction. According to the overall reaction ($CH_3OH + H_2O \xrightarrow{hv,catalyst} CO_2 + 3H_2$) in equation S8, the consumed methanol after 6 hours were determined to be 0.25 mmol and 0.65 mmol for C-TiO_2 and C-TiO_2/rGO, respectively, accounting for 0.004% and 0.01% of the total methanol initially spiked in the solution. Thus, the most possible cause for the H_2 production reached pseudo-equilibrium was the accumulation of H_2 in the overhead space of the photoreactor. That is why the photocatalytic reaction could be resumed by vacating H_2 from the solution via N_2 purge as shown in **Figure 9**.

View Article Online
DOI: 10.1039/C5RA26096E

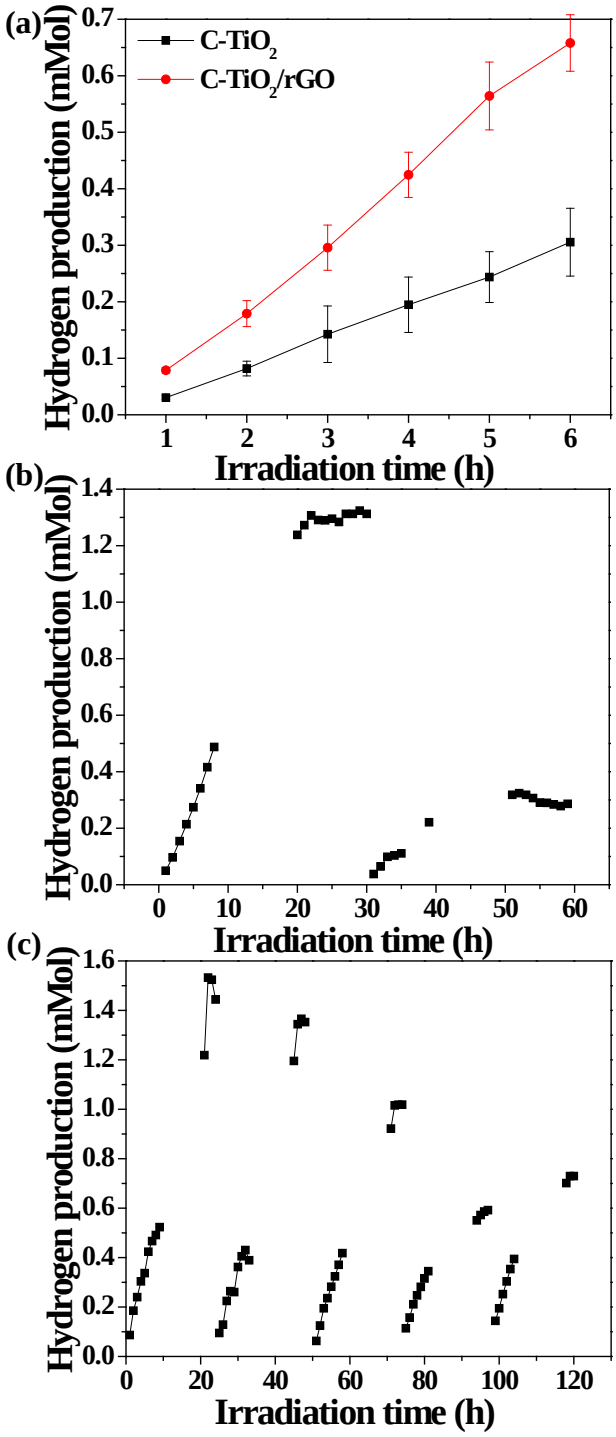

Figure 9. (a) Photocatalytic H_2 production kinetics by C-TiO_2 and C-TiO_2/rGO**.** (b-c) H_2 production for multiple reaction cycles by C-TiO_2 and C-TiO_2/rGO.

View Article Online
DOI: 10.1039/C5RA26096E

4. Conclusion

Tailored nanostructures offer a new way of facilitating electron–hole separation following excitation. Graphene-based nanomaterials offers additional opportunities to generate unique photocatalysts that demonstrated novel light absorption, thermodynamics, and stability. This work investigated a C-TiO_2 decorated onto rGO sheet, which yield enhanced photocatalytic activity and stability. The synthesized C-TiO_2 particles were in anatase phase with a band gap of 2.5 eV and thus could utilize visible light. The band gap further decreased to 2.2 eV after anchoring for C-TiO_2 to rGO. The H_2 production rate was also significantly increased for C-TiO_2/rGO compared to C-TiO_2. In addition to the effects on band structures and H_2 production, rGO decoration increased the longevity of photocatalytic reactions. The results confirm the beneficial roles of graphene sheets in facilitating charge separation and increasing photochemical or colloidal stability of photocatalysts. The new findings advanced the design of sustainable and efficient photocatalytic hybrid materials for renewable energy harvesting and environmental applications.

SUPPORTING INFORMATION

Table S1, Figure S1, and Synthesis of GO are included in ESI.

ACKNOWLEDGEMENT

This study was supported by the Research Startup Fund at NJIT and National Science Foundation Grant CBET-1235166. Authors thank Dr. Shijian Ge for the help and advice on experimental setup and appreciate the material characterization performed by Mr. Maocong Hu and Dr. Xianqin Wang in Department of Chemical Biological and Pharmaceutical Engineering at NJIT.

View Article Online
DOI: 10.1039/C5RA26096E

References:

1. L. Yan, J. Zhang, X. Zhou, X. Wu, J. Lan, Y. Wang, G. Liu, J. Yu and L. Zhi, *Int. J. Hydrogen Energy*, 2013, **38**, 3554-3561.
2. W. Yan, C. L. Zheng, Y. L. Liu and L. J. Guo, *Int. J. Hydrogen Energy*, 2011, **36**, 7405-7409.
3. H. Hagiwara, M. Nagatomo, C. Seto, S. Ida and T. Ishihara, *J. Photochem. Photobiol., A*, 2013, **272**, 41-48.
4. L. Kuang, Y. Zhao and L. Liu, *J. Environ. Monit.*, 2011, **13**, 2496-2501.
5. M. Radecka, M. Rekas, A. Trenczek-Zajac and K. Zakrzewska, *J. Power Sources*, 2008, **181**, 46-55.
6. P. D. Tran, S. K. Batabyal, S. S. Pramana, J. Barber, L. H. Wong and S. C. Loo, *Nanoscale*, 2012, **4**, 3875-3878.
7. T. Ikeda, T. Nomoto, K. Eda, Y. Mizutani, H. Kato, A. Kudo and H. Onishi, *J. Phys. Chem. C*, 2008, **112**, 1167-1173.
8. X. Chen and C. Burda, *J. Am. Chem. Soc.*, 2008, **130**, 5018-5019.
9. Y. Gai, J. Li, S.-S. Li, J.-B. Xia and S.-H. Wei, *Phys. Rev. Lett.*, 2009, **102**, 036402.
10. X. Chen and S. S. Mao, *Chem. Rev.*, 2007, **107**, 2891-2959.
11. D. Y. Leung, X. Fu, C. Wang, M. Ni, M. K. Leung, X. Wang and X. Fu, *Chem. Sus. Chem.*, 2010, **3**, 681-694.
12. X. Fan, X. Chen, S. Zhu, Z. Li, T. Yu, J. Ye and Z. Zou, *J. Mol. Catal. A: Chem.*, 2008, **284**, 155-160.
13. L. G. Devi, S. G. Kumar, B. N. Murthy and N. Kottam, *Catal. Commun.*, 2009, **10**, 794-798.
14. T. Ohno, T. Tsubota, Y. Nakamura and K. Sayama, *Applied Catalysis A: General*, 2005, **288**, 74-79.
15. J. L. Gole and J. D. Stout, *J. Phys. Chem. B*, 2004, **108**, 1230-1240.
16. A. P. Bhirud, S. D. Sathaye, R. P. Waichal, J. D. Ambekar, C.-J. Park and B. B. Kale, *Nanoscale*, 2015, **7**, 5023-5034.
17. R. Asahi, T. Morikawa, T. Ohwaki, K. Aoki and Y. Taga, *Science*, 2001, **293**, 269-271.
18. X. Chen, P.-A. Glans, X. Qiu, S. Dayal, W. D. Jennings, K. E. Smith, C. Burda and J. Guo, *J. Electron. Spectrosc. Relat. Phenom.*, 2008, **162**, 67-73.
19. C. Xu, Y. A. Shaban, W. B. Ingler and S. U. M. Khan, *Sol. Energ. Mat. Sol. Cells*, 2007, **91**, 938-943.
20. B. Liu, L.-M. Liu, X.-F. Lang, H.-Y. Wang, X. W. Lou and E. S. Aydil, *Energy Environ. Sci.*, 2014, **7**, 2592.
21. E. Barborini, A. M. Conti, I. Kholmanov, P. Piseri, A. Podestà, P. Milani, C. Cepek, O. Sakho, R. Macovez and M. Sancrotti, *Advanced materials*, 2005, **17**, 1842-1846.
22. V. Etacheri, M. K. Seery, S. J. Hinder and S. C. Pillai, *Inorg. Chem.*, 2012, **51**, 7164-7173.
23. X. Chen, S. Shen, L. Guo and S. S. Mao, *Chem. Rev.*, 2010, **110**, 6503-6570.
24. A. S. Barnard and P. Zapol, *Phys. Rev. B: Condens. Matter*, 2004, **70**, 235403.
25. X. Zhang, Y. Sun, X. Cui and Z. Jiang, *Int. J. Hydrogen Energy*, 2012, **37**, 811-815.
26. G. D. Moon, J. B. Joo, I. Lee and Y. Yin, *Nanoscale*, 2014, **6**, 12002-12008.
27. W.-J. Ong, M. M. Gui, S.-P. Chai and A. R. Mohamed, *RSC Adv.*, 2013, **3**, 4505-4509.
28. Y. Sang, Z. Zhao, J. Tian, P. Hao, H. Jiang, H. Liu and J. P. Claverie, *Small*, 2014, **10**, 3775-3782.
29. J. G. Radich, A. L. Krenselewski, J. Zhu and P. V. Kamat, *Chem. Mater.*, 2014, **26**, 4662-4668.
30. H.-i. Kim, S. Kim, J.-K. Kang and W. Choi, *J. Catal.*, 2014, **309**, 49-57.
31. Q. Huang, S. Tian, D. Zeng, X. Wang, W. Song, Y. Li, W. Xiao and C. Xie, *ACS Catal.*, 2013, **3**, 1477-1485.
32. X. Fu, Y. Liu, X. Cao, J. Jin, Q. Liu and J. Zhang, *Appl. Catal., B*, 2013, **130–131**, 143-151.
33. J. G. Radich and P. V. Kamat, *ACS Catal.*, 2012, **2**, 807-816.
34. F. Chen and N. J. Tao, *Acc. Chem. Res.*, 2009, **42**, 429-438.
35. T. Peng, K. Li, P. Zeng, Q. Zhang and X. Zhang, *J. Phys. Chem. C*, 2012, **116**, 22720-22726.
36. D. Wei and Y. Liu, *Adv. Mater.*, 2010, **22**, 3225-3241.

View Article Online
DOI: 10.1039/C5RA26096E

37. Y.-L. Min, K. Zhang, Y.-C. Chen and Y.-G. Zhang, *Sep. Purif. Technol.*, 2012, **86**, 98-105.
38. A. Mathkar, D. Tozier, P. Cox, P. Ong, C. Galande, K. Balakrishnan, A. Leela Mohana Reddy and P. M. Ajayan, *J. Phys. Chem. Lett.*, 2012, **3**, 986-991.
39. X.-Y. Zhang, H.-P. Li, X.-L. Cui and Y. Lin, *J. Mater. Chem.*, 2010, **20**, 2801-2806.
40. M.-Q. Yang, Y. Zhang, N. Zhang, Z.-R. Tang and Y.-J. Xu, *Sci. Rep.*, 2013, **3**, 3314.
41. X.-J. Lv, W.-F. Fu, H.-X. Chang, H. Zhang, J.-S. Cheng, G.-J. Zhang, Y. Song, C.-Y. Hu and J.-H. Li, *J. Mater. Chem.*, 2012, **22**, 1539.
42. F. Wang, M. Zheng, C. Zhu, B. Zhang, W. Chen, L. Ma and W. Shen, *Nanotechnology*, 2015, **26**, 345402.
43. P. Cheng, Z. Yang, H. Wang, W. Cheng, M. Chen, W. Shangguan and G. Ding, *Int. J. Hydrogen Energy*, 2012, **37**, 2224-2230.
44. W. Fan, Q. Lai, Q. Zhang and Y. Wang, *J. Phys. Chem. C*, 2011, **115**, 10694-10701.
45. H.-i. Kim, G.-h. Moon, D. Monllor-Satoca, Y. Park and W. Choi, *J. Phys. Chem. C*, 2012, **116**, 1535-1543.
46. S. G. Babu, R. Vinoth, D. P. Kumar, M. V. Shankar, H.-L. Chou, K. Vinodgopal and B. Neppolian, *Nanoscale*, 2015, **7**, 7849-7857.
47. Y. Li, C. Xie, S. Peng, G. Lu and S. Li, *Journal of Molecular Catalysis A: Chemical*, 2008, **282**, 117-123.
48. C. Han, Y. Wang, Y. Lei, B. Wang, N. Wu, Q. Shi and Q. Li, *Nano Research*, 2015, **8**, 1199-1209.
49. N. Vinothkumar and M. De, *Materials for Renewable and Sustainable Energy*, 2014, **3**, 1-10.
50. F. Pei, S. Xu, W. Zuo, Z. Zhang, Y. Liu and S. Cao, *International Journal of Hydrogen Energy*, 2014, **39**, 6845-6852.
51. W. Zhao, Z. Ai, J. Dai and M. Zhang, 2014.
52. H. Li, Y. Hao, H. Lu, L. Liang, Y. Wang, J. Qiu, X. Shi, Y. Wang and J. Yao, *Applied Surface Science*, 2015, **344**, 112-118.
53. B. Naik, S. Y. Moon, S. H. Kim and J. Y. Park, *Applied Surface Science*, 2015, **354, Part B**, 347-352.
54. K.-I. Liu, C.-Y. Su and T.-P. Perng, *RSC Advances*, 2015, **5**, 88367-88374.
55. B.-S. Huang and M.-Y. Wey, *International Journal of Hydrogen Energy*, 2011, **36**, 9479-9486.
56. S.-H. Liu and H.-R. Syu, *International Journal of Hydrogen Energy*, 2013, **38**, 13856-13865.
57. J. Gong, C. Yang, J. Zhang and W. Pu, *Applied Catalysis B: Environmental*, 2014, **152–153**, 73-81.
58. S. Sakthivel and H. Kisch, *Angewandte Chemie International Edition*, 2003, **42**, 4908-4911.
59. J. H. Park, S. Kim and A. J. Bard, *Nano letters*, 2006, **6**, 24-28.
60. H. Irie, Y. Watanabe and K. Hashimoto, *Chemistry Letters*, 2003, **32**, 772-773.
61. G. Wu, T. Nishikawa, B. Ohtani and A. Chen, *Chemistry of Materials*, 2007, **19**, 4530-4537.
62. E. M. Rockafellow, X. Fang, B. G. Trewyn, K. Schmidt-Rohr and W. S. Jenks, *Chemistry of Materials*, 2009, **21**, 1187-1197.
63. H. Wang, Z. Wu and Y. Liu, *The Journal of Physical Chemistry C*, 2009, **113**, 13317-13324.
64. N. Pinna, G. Garnweitner, M. Antonietti and M. Niederberger, *Journal of the American Chemical Society*, 2005, **127**, 5608-5612.
65. W. S. Hummers and R. E. Offeman, *J. Am. Chem. Soc.*, 1958, **80**, 1339-1339.
66. G. Zhang, W. Zhang, P. Wang, D. Minakata, Y. Chen and J. Crittenden, *Int. J. Hydrogen Energy*, 2013, **38**, 1286-1296.
67. G. Zhang, W. Zhang, D. Minakata, P. Wang, Y. Chen and J. Crittenden, *Int. J. Energy Res.*, 2014, **38**, 1513-1521.
68. G. Zhang, W. Zhang, J. Crittenden, D. Minakata, Y. Chen and P. Wang, *J. Renew. Sustain. Energy*, 2014, **6**, 033131.
69. W. Zhang, J. Crittenden, K. Li and Y. Chen, *Environ. Sci. Technol.*, 2012, **46**, 7054-7062.

View Article Online
DOI: 10.1039/C5RA26096E

70. S. Stankovich, D. A. Dikin, R. D. Piner, K. A. Kohlhaas, A. Kleinhammes, Y. Jia, Y. Wu, S. T. Nguyen and R. S. Ruoff, *Carbon*, 2007, **45**, 1558-1565.
71. M. Wang, J. Oh, T. Ghosh, S. Hong, G. Nam, T. Hwang and J.-D. Nam, *RSC Adv.*, 2014, **4**, 3284-3292.
72. C. Di Valentin, G. Pacchioni and A. Selloni, *Chemistry of Materials*, 2005, **17**, 6656-6665.
73. Z. Magdolenova, D. Bilaničová, G. Pojana, L. M. Fjellsbø, A. Hudecova, K. Hasplova, A. Marcomini and M. Dusinska, *Journal of Environmental Monitoring*, 2012, **14**, 455-464.
74. K. Suttiponparnit, J. Jiang, M. Sahu, S. Suvachittanont, T. Charinpanitkul and P. Biswas, *Nanoscale Res. Lett.*, 2011, **6**.
75. I. Chowdhury, N. D. Mansukhani, L. M. Guiney, M. C. Hersam and D. Bouchard, *Environmental science & technology*, 2015, **49**, 10886-10893.
76. R. Taziwa and E. Meyer, *Adv. Nanopart.*, 2014, **03**, 54-63.
77. X. Fan, W. Peng, Y. Li, X. Li, S. Wang, G. Zhang and F. Zhang, *Advanced materials*, 2008, **20**, 4490-4493.
78. K. Zhou, Y. Zhu, X. Yang, X. Jiang and C. Li, *New J. Chem.*, 2011, **35**, 353-359.
79. Z. Wang, B. Huang, Y. Dai, Y. Liu, X. Zhang, X. Qin, J. Wang, Z. Zheng and H. Cheng, *Cryst. Eng. Comm.*, 2012, **14**, 1687-1692.
80. L. Pan, J.-J. Zou, S. Wang, X.-Y. Liu, X. Zhang and L. Wang, *ACS Appl. Mater. Interfaces*, 2012, **4**, 1650-1655.
81. J. Shen, B. Yan, M. Shi, H. Ma, N. Li and M. Ye, *J. Mater. Chem.*, 2011, **21**, 3415-3421.
82. G. A. Tompsett, G. A. Bowmaker, R. P. Cooney, J. B. Metson, K. A. Rodgers and J. M. Seakins, *J. Raman Spectrosc.*, 1995, **26**, 57-62.
83. T. Ohsaka, F. Izumi and Y. Fujiki, *J. Raman Spectrosc.*, 1978, **7**, 321-324.
84. A. Lamberti, A. Chiodoni, N. Shahzad, S. Bianco, M. Quaglio and C. F. Pirri, *Sci. Rep.*, 2015, **5**.
85. B. Wang, H. Xin, X. Li, J. Cheng, G. Yang and F. Nie, *Sci. Rep.*, 2014, **4**.
86. S. Thakur and N. Karak, *Carbon*, 2012, **50**, 5331-5339.
87. G. T. S. How, A. Pandikumar, H. N. Ming and L. H. Ngee, *Scientific reports*, 2014, **4**.
88. C. Botas, P. Álvarez, C. Blanco, R. Santamaría, M. Granda, M. D. Gutiérrez, F. Rodríguez-Reinoso and R. Menéndez, *Carbon*, 2013, **52**, 476-485.
89. G. Zhang, W. Zhang, D. Minakata, Y. Chen, J. Crittenden and P. Wang, *Int. J. Hydrogen Energy*, 2013, **38**, 11727-11736.
90. J. Ding, W. Yan, W. Xie, S. Sun, J. Bao and C. Gao, *Nanoscale*, 2014, **6**, 2299-2306.
91. K.-Y. Lian, Y.-F. Ji, X.-F. Li, M.-X. Jin, D.-J. Ding and Y. Luo, *J. Phys. Chem. C*, 2013, **117**, 6049-6054.
92. T.-F. Yeh, J.-M. Syu, C. Cheng, T.-H. Chang and H. Teng, *Adv. Funct. Mater.*, 2010, **20**, 2255-2262.
93. H. Yan, X. Wang, M. Yao and X. Yao, *Prog. Nat. Sci.*, 2013, **23**, 402-407.
94. K. Palanivelu, J. S. Im and Y.-S. Lee, *Carbon Science*, 2007, **8**, 11.
95. D. Yang, L. Zhou, L. Chen, B. Zhao, J. Zhang and C. Li, *Chem. Commun.*, 2012, **48**, 8078-8080.
96. M. Reza Gholipour, C.-T. Dinh, F. Beland and T.-O. Do, *Nanoscale*, 2015, **7**, 8187-8208.
97. T. Tachikawa, S. Tojo, K. Kawai, M. Endo, M. Fujitsuka, T. Ohno, K. Nishijima, Z. Miyamoto and T. Majima, *J. Phys. Chem. B*, 2004, **108**, 19299-19306.
98. Y. Zhang, N. Zhang, Z.-R. Tang and Y.-J. Xu, *ACS Nano*, 2012, **6**, 9777-9789.
99. H. Zhang, X. Lv, Y. Li, Y. Wang and J. Li, *ACS Nano*, 2010, **4**, 380-386.
100. X. Wang, L. Zhi and K. Müllen, *Nano Lett.*, 2008, **8**, 323-327.
101. J. Puskelova, L. Baia, A. Vulpoi, M. Baia, M. Antoniadou, V. Dracopoulos, E. Stathatos, K. Gabor, Z. Pap, V. Danciu and P. Lianos, *Chem. Eng. J.*, 2014, **242**, 96-101.
102. F. Sordello and C. Minero, *Appl. Catal., B*, 2015, **163**, 452-458.
103. H. Li, X. Zhang and X. Cui, *Int. J. Photoenergy*, 2014, **2014**, 9.

View Article Online
DOI: 10.1039/C5RA26096E

Carbon doped TiO_2 anchored to reduced graphene oxide formed a hybrid nanocomposite (C-TiO_2/rGO) that exhibited greater photocatalytic activity and stability.